Fluid pumping by liquid metal droplet utilizing ac electric field

Chun-Lei Song,[1] Ye Tao,[1,2,*] Wei-Yu Liu,[3] Yi-Cheng Chen,[4] Rui Xue,[1] Tian-Yi Jiang,[5] Biao Li,[4] Hong-Yuan Jiang,[5] and Yu-Kun Ren[1,†]

[1]*State Key Laboratory of Robotics and System, Harbin Institute of Technology, Harbin 150001, China*
[2]*School of Engineering and Applied Sciences and Department of Physics, Harvard University, Cambridge, Massachusetts 02138, USA*
[3]*School of Electronics and Control Engineering, Chang'an University, Xi'an 710000, China*
[4]*School of Energy Science and Engineering, Harbin Institute of Technology, Harbin 150001, China*
[5]*School of Mechatronics Engineering, Harbin Institute of Technology, Harbin 150001, China*

(Received 19 June 2021; revised 21 October 2021; accepted 25 January 2022; published 8 February 2022)

We report a unique phenomenon in which liquid metal droplets (LMDs) under a pure ac electric field pump fluid. Unlike the directional pumping that occurs upon reversing the electric field polarity under a dc signal, this phenomenon allows the direction of fluid motion to be switched by simply shifting the position of the LMD within the cylindrical chamber. The physical mechanism behind this phenomenon has been termed Marangoni flow, caused by nonlinear electrocapillary stress. Under the influence of a localized, asymmetric ac electric field, the polarizable surface of the position-offset LMD produces a net time-averaged interfacial tension gradient that scales with twice the field strength, and thus pumps fluid unidirectionally. However, the traditional linear *RC* circuit polarization model of the LMD/electrolyte interface fails to capture the correct pump-flow direction when the thickness of the LMD oxide skin is non-negligible compared to the Debye length. Therefore, we developed a physical description by treating the oxide layer as a distributed capacitance with variable thickness and connected with the electric double layer. The flow profile is visualized via microparticle imaging velocimetry, and excellent consistency is found with simulation results obtained from the proposed nonlinear model. Furthermore, we investigate the effects of relevant parameters on fluid pumping and discuss a special phenomenon that does not exist in dc control systems. To our knowledge, no previous work addresses LMDs in this manner and uses a zero-mean ac electric field to achieve stable, adjustable directional pumping of a low-conductivity solution.

DOI: 10.1103/PhysRevE.105.025102

I. INTRODUCTION

The eutectic alloy of gallium-indium (EGaIn, 75% gallium, 25% indium), a kind of room-temperature liquid metal, has attracted increasing interest owing to its potential applications in stretchable electronics [1–4], 3D printing [5,6], sensors [7,8], microfluidic chips [9–11], etc. The applicability of this material to such fields stems from the excellent material properties of liquid metals, containing metallic conductivity (3.4×10^6 S/m), a viscosity (1.99×10^{-3} Pa s) similar to that of water (1×10^{-3} Pa s), nontoxicity relative to mercury, and rich surface chemistry [9,12–15]. In addition, interfacial tension plays a vital role in several small-length-scale systems. For example, adjusting the interfacial tension allows liquid metal droplets (LMDs) to be merged and separated, which enables their use in shape-reconfigurable electronics applications [16].

LMD interfacial tension gradients can arise from a variety of causes, including spatial variations in the electric charge or surface potential [17–19], the electrolyte ion content [20,21], and surface oxidation [22] at the interface. Of these, the electric field is one of the most efficient and flexible physical stimuli for regulation of LMD interfacial tension because its magnitude, phase, and frequency can be adjusted easily. In recent years, many scientists and engineers have manipulated LMDs for various functions and applications. First, Tang *et al.* [23] proposed a liquid-metal-driven pump and demonstrated that a LMD in an electrolyte-filled channel pumps fluid during exposure to a dc-biased square wave. It is worth noting that the purpose of the ac electric field is to avoid oxide layer formation. More recently, there has been extensive research on other behavior that can be activated using a dc electric field, such as motion [24–26] and the heart beating effect [27–30]. The use of an ac electric field to manipulate LMDs has also been studied. Tang *et al.* [31] achieved fluid mixing under an ac electric field via induced harmonic Marangoni flow around the LMD, and explained the phenomenon both theoretically and experimentally. However, LMDs oxidize easily to form oxide layers. The passivating and electrically insulating oxide causes the electrocapillary phenomenon to weaken dramatically or even disappear [32]. Therefore, to eliminate the influence of the oxide layer on the LMD surface, the electrolytes that surround the LMDs in most studies include high-concentration alkaline solutions (>6 S/m, 0.3 M), which are pretty inappropriate for biomedical applications. In fact, ac electric fields provide an alternative approach to inhibiting oxide layer formation. Thus, it is feasible to utilize this mode to govern EGaIn droplets within a low-conductivity NaOH solution.

In this study, we employed ac electric fields to control the electrochemical polarization of EGaIn droplets. Stable and

*Corresponding author: ytao@seas.harvard.edu
†Corresponding author: rykhit@hit.edu.cn

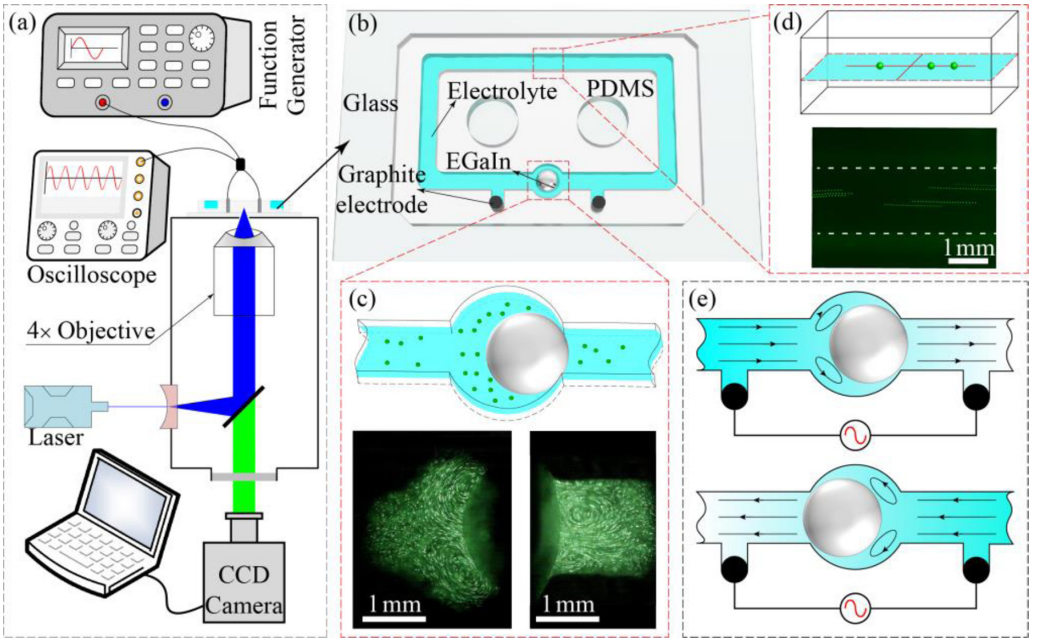

FIG. 1. Sketch of the present experimental setup and the typical outcomes for the pumping fluid: (a) the experimental setup; (b) 3D schematic of the fluidic chip; images obtained from the camera for (c) visualization of flow profile around the EGaIn droplet and (d) calculating the flow velocity in the middle section of the channel; (e) schematic diagram of direction-controllable pumping by moving the location of the droplet.

unidirectional fluid pumping was realized by the ac electrocapillary effect when a harmonically varying voltage signal was applied, and the EGaIn droplet was positioned asymmetrically within the cylindrical chamber. Unlike conventional DC electrocapillary flow derived from the linear component of the interfacial stress [33], electrolyte pumping via ac forcing occurs due to asymmetry breaking in the spatial distribution of the nonlinear electrocapillary stress of the second-order voltage dependence.

A physical description of ac electrocapillary pumping fluid was developed from the perspective of induced-charge electrokinetic phenomena, wherein the oxide layer is embedded as a distributed capacitor with a continuously varying thickness that is dependent on the local electric field, frequency, and solution conductivity. When using a low-conductivity NaOH solution ($\sigma_f < 1.6\,\mathrm{S/m}$), the oxide skin is removed more slowly than it is generated via electrochemical oxidation. Thus, oxide-layer deposition occurs on the conducting droplet surface, and the traditional simplified model that ignores the oxidation effect fails. An improved theoretical treatment predicts the correct pump direction, as the appearance of an oxide layer of nonuniform thickness inverts the double-layer potential drop gradient and thereby forms nonlinear bipolar electrocapillary stress of the desired asymmetry. In other words, although the EGaIn droplet oxide skin reduces the interfacial tension, it also changes the interfacial tension gradient due to the uneven voltage division. Upon increasing the NaOH concentration ($1.6 \leqslant \sigma_f \leqslant 5.3\,\mathrm{S/m}$), flow reversal is observed experimentally within a certain electric field frequency range. Implementation of the new model allows this behavior to be reconstructed qualitatively via numerical prediction.

II. EXPERIMENTAL METHOD AND NUMERICAL SIMULATION DETAILS

A. Micro-PIV experiments

Figure 1(a) shows our experimental setup, which consisted of four parts: a function generator (TGA12104, TTi, UK), oscilloscope (Tektronix, 2014B, USA), fluidic chip, and microparticle imaging velocimetry (micro-PIV) system. The ac sinusoidal signals, which were generated using a function generator, acted on the EGaIn droplet surrounded by an electrolyte solution through the graphite electrode. Meanwhile, an oscilloscope was used to monitor the actual output waveform. The flow pattern visualization and velocity measurement were performed via micro-PIV, which tracks the displacement of a collection of tracer particles to characterize flow fields within microfluidic devices [34–36]. The micro-PIV system included a CCD camera (V7.3, Phantom, USA), fluorescent inverted microscope (IX71, Olympus, Japan), and laser (Mini-YAG Y50-15, New Wave, USA). We used polystyrene (PS) fluorescent microspheres (G0500, Duke, USA) with an average diameter of 5 μm as tracer particles. The particle concentration was $\sim 0.04\%$. A fluidic chip was fabricated by bonding polydimethylsiloxane (PDMS) with glass, and the PDMS channel was polymerized using a polymethylmethacrylate (PMMA) pattern as a mold. The device fabrication process is shown in detail in Fig. S1 (in Supplemental Material [37]). The PDMS channel consisted of three parts: a closed-loop, open-top rectangular fluidic channel with a cross section of $1.66 \times 3\mathrm{mm}^2$; a cylindrical chamber with a diameter of 4 mm for accommodating an EGaIn droplet; and a pair of holes with 2 mm diameters and a center distance of 15 mm designed to hold the graphite electrode as shown in Fig. 1(b). We first

observed the fluid flow around the droplet to explore the fluid pumping mechanism and obtained vector fields using the PIV software to cross-correlate consecutive images, as shown in Fig. 1(c). Then, the channel axis velocity was measured to evaluate the pumping performance, as shown in Fig. 1(d). Upon application of an ac electrical field, an EGaIn droplet located adjacent to the cylindrical chamber (on either outlet) was subjected to a nonuniform electric field due to symmetry breaking in the geometric configuration. This phenomenon resulted in an asymmetric bipolar interfacial tension gradient at the EGaIn/electrolyte interface, which led to fluid flow around the droplet, i.e., Marangoni flow driven by nonlinear electrocapillary stress. When the EGaIn droplet position was changed, the gradient of interfacial tension changed in polarity, and the direction of the pump fluid motion reversed, as shown in Fig. 1(e).

B. Theoretical background

1. Charge distribution

When an EGaIn droplet is immersed in the NaOH solution, the EGaIn surface carries a negative charge distribution because the $[Ga(OH)_4]^-$ ion is formed by the chemical reaction between gallium and an alkali solution. This negative surface charge attracts cations from the solution and repels anions via diffuse charge dynamics to create an electrochemical electric double layer (EDL) at the droplet/solution interface. Notably, this process is spontaneous and does not require an external electric field. Thus, we refer to the resulting electrochemical double layer as the original electric double layer (OEDL). Furthermore, the OEDL can be equivalent to a dielectric capacitor, and the electrostatic potential ΔU_{OEDL} difference across an OEDL full of unipolar cations (external minus internal) created by the uniformly distributed negative surface charge can be expressed as,

$$\Delta U_{\mathrm{OEDL}} = -\frac{q_0}{C_{\mathrm{DL}}}, \tag{1}$$

where $q_0 = -0.05$ C/m^2 [23,38] is the native surface free charge density and $C_{\mathrm{DL}} = C_S C_D/(C_S + C_D)$ represents the OEDL capacitance per unit area. The later quantity consists of the Stern-layer capacitance $C_S = 0.8$ F/m^2 [33,39,40] of immobile ions and the diffuse-layer capacitance $C_D = \varepsilon_f/\lambda_d$ of mobile counterions in series, where the dielectric permittivity of water is ε_f and the Debye length $\lambda_d = \sqrt{D\varepsilon_f/\sigma_f}$ [41]. Here, $D = 2 \times 10^{-9}$ m^2/s is the diffusivity coefficient of NaOH, as estimated using the Einstein equation [42], and σ_f is the conductivity of the electrolyte solution.

The EGaIn droplet behaves as an ideally polarizable object when suspended in an electrolyte because of its inherent high conductivity. When an electric field is applied, charge rearranges along the droplet surface, resulting in the formation of an induced double layer (IDL) of bipolar counterions that are superimposed onto the OEDL. Since the droplet surface automatically acquires a negative surface charge distribution, charge addition within the IDL and OEDL causes more cations to accumulate on the hemisphere surface near the anode than the cathode. This leads to the formation of a final electric double layer (FEDL) with an asymmetric charge distribution. Within the framework of the FEDL, the IDL formed in the electrolyte is full of bipolar counterions and can be modeled as a plate capacitor called the Helmholtz-Perrin model [23,43]. At the EGaIn droplet surface, the normal Ohmic current in the electrolyte solution phase charges the IDL like a capacitor skin, which meets the current continuity condition, i.e., the normal Ohmic current from the solution resistance is equal to the displacement current flowing within the IDL capacitor,

$$\mathbf{n} \cdot (\sigma_f \nabla \tilde{\phi}) = j\omega C_T (\tilde{\phi} - \tilde{\phi}_{\mathrm{drop}}), \tag{2}$$

where $\mathbf{n}$ is the normal unit vector; j is the imaginary unit; ω is the angular frequency of the electric field; the tilde $\sim$ represents the complex form of the sinusoidal electric field; ϕ is the electrical potential in the electrolyte bulk right outside the Debye layer formed on the conducting surface; ϕ_{drop} is the equal-body potential of the EGaIn droplet, which is affected by the background ac signal; and $C_T = \frac{C_{\mathrm{DL}}C_{ox}}{C_{\mathrm{DL}}+C_{ox}} = \frac{C_s C_D C_{ox}}{C_s C_D + C_s C_{ox} + C_D C_{ox}}$ is the total interfacial capacitance per unit area. The latter quantity is formed from the Stern, diffuse, and oxide layer capacitances connected in series. The dielectric capacitance C_{ox} is given as

$$C_{ox} = \frac{\varepsilon_{\mathrm{ox}}}{d_{ox}}, \tag{3}$$

where ε_{ox} and d_{ox} are the dielectric permittivity and thickness, respectively, of the oxide layer.

An EGaIn droplet immersed in an electrolyte such as NaOH is oxidized electrochemically to form an oxide layer when subject to an electric field [22,44]. The main component of the oxide layer is Ga_2O_3 [21], which can dissolve in a concentrated NaOH solution to form $NaGa(OH)_4$. Thus, application of a potential drive oxide deposition, which competes with oxide dissolution [16]. In addition, the oxide layer thickness is compromised because there is insufficient time for oxidation in a high-frequency ac electric field [16,19]. In other words, the voltage plays a positive role in forming the oxide layer, while the frequency and solution conductivity have opposite effects. The thickness of the oxide layer d_{ox} is directly proportional to the electric field intensity and inversely proportional to the frequency and conductivity. That is, $d_{ox} \propto \mathbf{E}/\sigma_f f$. Based on the principle of dimensional homogeneity and scaling theory, we introduced the proportionality coefficient α, whose value ranges from 10^{-10} to 10^{-9} because the thickness of the oxide layer is less than 10 nm [13]. The solubility of the electrolyte in the oxide layer should be considered when selecting the proportionality coefficient α. Based on the above analysis, the thickness of the oxide layer d_{ox} is defined as

$$d_{ox} = \frac{\alpha}{\sqrt{0.5}} \frac{\sqrt{\langle \mathbf{E}^2(t) \rangle}}{\sigma_f f} = \frac{\alpha\sqrt{0.5\tilde{\mathbf{E}}\tilde{\mathbf{E}}^*}}{\sqrt{0.5}\sigma_f f} = \frac{\alpha\sqrt{\tilde{\mathbf{E}}\tilde{\mathbf{E}}^*}}{\sigma_f f}, \tag{4}$$

where α is the proportionality coefficient, $\mathbf{E}(t)$ is the electric field intensity, t is the time, $\langle \mathbf{E}^2(t) \rangle$ denotes the time-averaged value of $\mathbf{E}^2(t)$ within a complete ac voltage cycle, * indicates a complex conjugate, and f is the electric field frequency.

Since the Dukhin number is sufficiently small, the total potential drop across the double layer can be calculated according to the linear superimposition principle within the

Debye-Hückel limit:

$$\Delta U_{\mathrm{IDL}}(t) = \frac{C_T}{C_{\mathrm{DL}}}\mathrm{Re}((\tilde{\phi} - \tilde{\phi}_{\mathrm{drop}})\exp(j\omega t)), \tag{5a}$$

$$\Delta U_{\mathrm{FEDL}}(t) = \Delta U_{\mathrm{OEDL}}(t) + \Delta U_{\mathrm{IDL}}(t) = -\frac{q_0}{C_{\mathrm{DL}}} + \frac{C_T}{C_{\mathrm{DL}}}\mathrm{Re}((\tilde{\phi} - \tilde{\phi}_{\mathrm{drop}})\exp(j\omega t)). \tag{5b}$$

2. Marangoni flow

The electric field causes charge redistribution at the polarized structural interface, which changes the potential difference across the FEDL. The interfacial tension of the EGaIn droplet then adjusts accordingly. The relationship between the voltage drop and interfacial tension satisfies the Lippmann equation,

$$\gamma(t) = \gamma_0 - \frac{1}{2}C_{\mathrm{DL}}[\Delta U_{\mathrm{FEDL}}(t)]^2 = \gamma_0 - \frac{1}{2}C_{\mathrm{DL}}\left[-\frac{q_0}{C_{\mathrm{DL}}} + \frac{C_T}{C_{\mathrm{DL}}}\mathrm{Re}((\tilde{\phi} - \tilde{\phi}_{\mathrm{drop}})\exp(j\omega t))\right]^2 \tag{6a}$$

with the time-averaged counterpart

$$\langle\gamma(t)\rangle = \frac{1}{T}\int_0^T \gamma(t)dt = \gamma_0 - \frac{1}{2}C_{\mathrm{DL}}\left[\left(\frac{q_0}{C_{\mathrm{DL}}}\right)^2 + \frac{1}{2}\left(\frac{C_T}{C_{\mathrm{DL}}}\right)^2(\tilde{\phi} - \tilde{\phi}_{\mathrm{drop}})(\tilde{\phi} - \tilde{\phi}_{\mathrm{drop}})^*\right] \tag{6b}$$

where γ is the interfacial tension and γ_0 is the maximum interfacial tension at $\Delta U_{\mathrm{FEDL}}(t) = 0$.

The interfacial tension varies along the surface in a nonuniform electric field activated by driving electrodes. In other words, the interfacial tension gradient is not zero. Thus, tangential stress is applied on the surface, resulting in a surface drag force that acts on the adjacent fluid. This force eventually causes fluid movement, which is usually referred to as Marangoni flow [45–47], in the channel. The tangential stress is given by

$$\tau_{\mathbf{E}} = \nabla_t\gamma, \tag{7}$$

where $\tau_{\mathbf{E}}$ is the tangential hydrodynamic stress and ∇_t denotes the surface gradient. Equation (7) implies that the fluid tends to flow from lower to higher interfacial tension.

3. One-dimension analytical approximation

The complete system is so complex that the solution is nontrivial. To better characterize the Marangoni flow under an ac electric field, we calculated the approximate analytical solution based on the assumption that the EGaIn droplet is infinitely long in the x direction. Given a complex excitation voltage V_0 and an interelectrode distance L, the background electric field intensity is $\mathbf{E} = V_0/L$.

A local voltage drop of $-\mathbf{E}x$ is present across the series circuit of the capacitor skin and the electrolyte bulk adjacent to the EGaIn droplet. In this equation, x denotes the axial distance from the centroid of droplet to the point of interest on the conducting surface. Impedance analysis provides the voltage component $\tilde{\phi} - \tilde{\phi}_{\mathrm{drop}}$ within C_T,

$$\tilde{\phi} - \tilde{\phi}_{\mathrm{drop}} = \frac{-\mathbf{E}x}{1 + j\omega\frac{C_T R}{\sigma_f}}, \tag{8}$$

where R is the characteristic size of the EGaIn droplet, which is assumed equal to the droplet radius.

Substituting Eq. (8) into Eq. (6) produces a more explicit form of the voltage-dependent interfacial tension coefficient:

$$\gamma(t) = \gamma_0 - \frac{1}{2}C_{\mathrm{DL}}[\Delta U_{\mathrm{FEDL}}(t)]^2 = \gamma_0 - \frac{1}{2}C_{\mathrm{DL}}\left[-\frac{q_0}{C_{\mathrm{DL}}} + \frac{C_T}{C_{\mathrm{DL}}}\mathrm{Re}\left(\frac{-\mathbf{E}x}{1 + j\omega\frac{C_T R}{\sigma_f}}\exp(j\omega t)\right)\right]^2$$
$$= \gamma_0 - \frac{1}{2}C_{\mathrm{DL}}\left\{\left(\frac{q_0}{C_{\mathrm{DL}}}\right)^2 + \frac{1}{2}\left(\frac{C_T}{C_{\mathrm{DL}}}\right)^2\frac{\mathbf{E}^2x^2}{1 + \left(\omega\frac{C_T R}{\sigma_f}\right)^2} + \left(\frac{C_T}{C_{\mathrm{DL}}}\right)^2\frac{\mathbf{E}^2x^2}{\left[1 + \left(\omega\frac{C_T R}{\sigma_f}\right)^2\right]^2}\right.$$
$$\left.\times\left[\frac{1 - \left(\omega\frac{C_T R}{\sigma_f}\right)^2}{2}\cos(2\omega t) + \omega\frac{C_T R}{\sigma_f}\sin(2\omega t)\right] + \frac{2q_0}{C_{\mathrm{DL}}}\frac{C_T}{C_{\mathrm{DL}}}\frac{\mathbf{E}x}{1 + \left(\omega\frac{C_T R}{\sigma_f}\right)^2}\left[\cos(\omega t) + \omega\frac{C_T R}{\sigma_f}\sin(\omega t)\right]\right\}. \tag{9}$$

The ratio of the surface capacitive reactance of the electrical double layer to the total interfacial capacitance is

$$\frac{C_T}{C_{\mathrm{DL}}} = \frac{C_o}{C_{\mathrm{DL}} + C_o} = \frac{\varepsilon_{ox}\Big/\frac{\alpha\sqrt{\tilde{\mathbf{E}}\tilde{\mathbf{E}}^*}}{\sigma_f f}}{C_{\mathrm{DL}} + \varepsilon_{ox}\Big/\frac{\alpha\sqrt{\tilde{\mathbf{E}}\tilde{\mathbf{E}}^*}}{\sigma_f f}}. \tag{10}$$

Although C_T/C_{DL} is a decreasing function of the local electric field strength, the surface gradient of the interfacial tension in Eq. (9) along the x axis direction is calculated by assuming a constant C_T/C_{DL}:

$$\frac{\partial\gamma(t)}{\partial x} = -\frac{1}{4}\left(\frac{C_T}{C_{\mathrm{DL}}}\right)^2\frac{2\mathbf{E}^2x}{1 + \left(\omega\frac{C_T R}{\sigma_f}\right)^2} - \frac{1}{2}C_{\mathrm{DL}}\left(\frac{C_T}{C_{\mathrm{DL}}}\right)^2\frac{2\mathbf{E}^2x}{\left[1 + \left(\omega\frac{C_T R}{\sigma_f}\right)^2\right]^2}\left[\frac{1 - \left(\omega\frac{C_T R}{\sigma_f}\right)^2}{2}\cos(2\omega t) + \omega\frac{C_T R}{\sigma_f}\sin(2\omega t)\right]$$
$$- q_0\frac{C_T}{C_{\mathrm{DL}}}\frac{\mathbf{E}}{1 + \left(\omega\frac{C_T R}{\sigma_f}\right)^2}\left[\cos(\omega t) + \omega\frac{C_T R}{\sigma_f}\sin(\omega t)\right]. \tag{11}$$

Equation (11) can be decomposed further into a combination of a time-averaged steady component, transient forcing at the frequency of the imposed ac voltage, and another transient component that oscillates at twice the electric field frequency:

$$\left\langle \frac{\partial \gamma(t)}{\partial x} \right\rangle = -\frac{1}{4} C_{\mathrm{DL}} \left(\frac{C_T}{C_{\mathrm{DL}}} \right)^2 \frac{2\mathbf{E}^2 x}{1 + \left(\omega \frac{C_T R}{\sigma_f}\right)^2}, \tag{12a}$$

$$\left(\frac{\partial \gamma(t)}{\partial x} \right)_{\omega} = -q_0 \frac{C_T}{C_{\mathrm{DL}}} \frac{\mathbf{E}}{1 + \left(\omega \frac{C_T R}{\sigma_f}\right)^2} \left(\cos(\omega t) + \omega \frac{C_T R}{\sigma_f} \sin(\omega t) \right), \tag{12b}$$

$$\left(\frac{\partial \gamma(t)}{\partial x} \right)_{2\omega} = -\frac{1}{2} C_{\mathrm{DL}} \left(\frac{C_T}{C_{\mathrm{DL}}} \right)^2 \frac{2\mathbf{E}^2 x}{\left[1 + \left(\omega \frac{C_T R}{\sigma_f}\right)^2\right]^2} \left[\frac{1 - \left(\omega \frac{C_T R}{\sigma_f}\right)^2}{2} \cos(2\omega t) + \omega \frac{C_T R}{\sigma_f} \sin(2\omega t) \right], \tag{12c}$$

When $\frac{C_T}{C_{\mathrm{DL}}} \to 1$, the term $-\mathbf{E}^2 x$ determines the main trait of the resulting nonlinear electrocapillary flow behavior. This requires that

$$\frac{\varepsilon_{ox}}{\frac{\alpha \sqrt{\tilde{\mathbf{E}}\tilde{\mathbf{E}}^*}}{\sigma_f f}} > C_{\mathrm{DL}}, \quad \text{viz.}, \; f > \frac{\alpha |\mathbf{E}| C_{\mathrm{DL}}}{\varepsilon_{ox} \sigma_f}. \tag{13}$$

That is, for $f > |\mathbf{E}| C_{\mathrm{DL}} / \varepsilon_{ox} \sigma_f = f_{\mathrm{crossover}}$, $C_T / C_{\mathrm{DL}} = 1$, C_{ox} is negligible, and $-\mathbf{E}^2 x$ controls the direction of the bipolar electrokinetic vortex flow at the EGaIn/electrolyte interface. In this situation, the electric field $\mathbf{E}$ is stronger for $x > 0$ than that for $x < 0$ when the EGaIn droplet is located adjacent to the right outlet of the cylindrical chamber. The counterclockwise-rotating eddy on the surface of the right hemisphere dominates its clockwise-rotating counterpart on the left side. Thus, the net pump flow is oriented from the right to left of the EGaIn droplet when the droplet is located near the right chamber outlet. We call this situation negative pumping mode or "−" pumping mode. This "−" pumping mode also includes the phenomenon of rightward pump motion when the droplet is positioned near the left chamber outlet. On the other hand, if $\varepsilon_{ox} / \frac{\alpha \sqrt{\tilde{\mathbf{E}}\tilde{\mathbf{E}}^*}}{\sigma_f f} < C_{\mathrm{DL}}$ or $f < \alpha |\mathbf{E}| C_{\mathrm{DL}} / \varepsilon_{ox} \sigma_f$, the pump stress behavior is determined mainly by the specific value of C_T / C_{DL}. In other words, the voltage division of oxide layer plays a critical role. Although a strong local electric field exists within the thin slit, C_T / C_{DL} is smaller on the side of droplet near the slit than on the other side, resulting in a slower vortex flow around the slit. Thus, the net fluid flows towards the slit from the other side of the LMD. This situation is called positive pump mode or "+" pumping mode.

With the definition of the two opposite pumping modes, considering the synergy of electrode polarization, varying oxide layer thickness, and relaxation of electrochemical ion around the IDL, the pump-flow direction should obey the rules given in Tables I and II for low- and high-conductivity solutions, respectively.

The frequency dispersion curves of the longitudinal pump flow velocity are plotted qualitatively in Figs. 5(c1) and 5(c2) for the two distinct low and high conductivity regimes, respectively. In practice, unlike in the theoretical prediction, it is usually impossible to observe the occurrence of weak "−" pumping behavior at $f > \alpha \mathbf{E} C_{\mathrm{DL}} / \varepsilon_{ox} \sigma_f$ within a low conductivity environment. This is because double-layer charge relaxation at $f > \sigma_f / 2\pi C_T R$ already produces almost no voltage drop across the IDL capacitance, leading to a diminishing interfacial tension gradient.

C. Numerical simulation methodology

The commercial finite-element-method-based software package COMSOL MULTIPHYSICS 5.5 (COMSOL AB, Stockholm, Sweden), was employed in order to reconstruct the phenomenon of Marangoni flow driven by nonlinear bipolar electrocapillary stress [Eq. (6b) or (12)] at the conducting surface of the EGaIn droplet. The 3D geometry in Fig. S2 (in Supplemental Material [37]) was created using the "Geometry" tool in the simulation. The physics interfaces used in the solution included "Electric Currents" and "Laminar Flow." Further details of the governing equations and their corresponding boundary conditions are shown in Supplemental Material [37]. The electric field equation was recast in the frequency domain to acquire a complex potential phasor, and the steady-state ac electrocapillary flow field was solved using a stationary solver. In solver configurations, a single physics field was solved directly, and the fully coupled method

TABLE I. Frequency-dependent analytical pump flow behavior at low liquid conductivities.

Conductivity range	$\sigma_f < \sqrt{\frac{\alpha \mathbf{E} C_{\mathrm{DL}} C_T 2\pi R}{\varepsilon_{ox}}}$			
Frequency range	$0 < f < \frac{\sigma_f}{2\pi C_{\mathrm{DL}} R}$	$\frac{\sigma_f}{2\pi C_{\mathrm{DL}} R} \leqslant f \leqslant \frac{\sigma_f}{2\pi C_T R}$	$\frac{\sigma_f}{2\pi C_T R} < f \leqslant \frac{\alpha \mathbf{E} C_{\mathrm{DL}}}{\varepsilon_{ox} \sigma_f}$	$f > \frac{\alpha \mathbf{E} C_{\mathrm{DL}}}{\varepsilon_{ox} \sigma_f}$
Pumping mode	weak "+"	efficient "+"	weak "+"	weak "−"
Scaling trait	$\propto \sigma_f \mathbf{E}^k (0 < k < 1)$	$\propto \sigma_f \mathbf{E}^k (0 < k < 1)$	$\propto \sigma_f \mathbf{E}^k (0 < k < 1)$	$\propto \sigma_f{}^0 \mathbf{E}^2$
Dominant factor	Electrode polarization and surface oxidation	Surface oxidation	Surface oxidation	Nonlinear electrocapillary stress
Surface vortex flow	Diverging	Diverging	Diverging	Converging

TABLE II. Frequency-dependent analytical pump flow behavior at high liquid conductivities.

Conductivity range	$\sigma_f > \sqrt{\frac{\alpha \mathbf{E} C_{\mathrm{DL}} C_T 2\pi R}{\varepsilon_{ox}}}$			
Frequency range	$0 < f < \frac{\sigma_f}{2\pi C_{\mathrm{DL}} R}$	$\frac{\sigma_f}{2\pi C_{\mathrm{DL}} R} \leqslant f \leqslant \frac{\alpha \mathbf{E} C_{\mathrm{DL}}}{\varepsilon_{ox}\sigma_f}$	$\frac{\alpha \mathbf{E} C_{\mathrm{DL}}}{\varepsilon_{ox}\sigma_f} < f \leqslant \frac{\sigma_f}{2\pi C_T R}$	$f > \frac{\sigma_f}{2\pi C_T R}$
Pumping mode	weak "+"	efficient "+"	efficient "−"	weak "−"
Scaling trait	$\propto \sigma_f \mathbf{E}^k (0 < k < 1)$	$\propto \sigma_f \mathbf{E}^k (0 < k < 1)$	$\propto {\sigma_f}^0 \mathbf{E}^2$	$\propto {\sigma_f}^0 \mathbf{E}^2$
Dominant factor	Electrode polarization and surface oxidation	Surface oxidation	Nonlinear electrocapillary stress	Nonlinear electrocapillary stress
Surface vortex flow	Diverging	Diverging	Converging	Converging

was used between these physical fields. We selected a free tetrahedral mesh with moderate size (709720) after performing a trade-off between numerical accuracy and the cost of computation (Fig. S3, in Supplemental Material [37]).

III. RESULTS AND DISCUSSION

During the experiment, we observed fluid pumping, as well as EGaIn droplet oscillation and deformation. The fluid pumping phenomenon consists of codirectional pumping ("+" pumping mode) and reverses pumping ("−" pumping mode). In "+" mode, the fluid flows to the right (left) when the droplet is close to the right (left) chamber outlet (Video S1, in Supplemental Material [37]). The "−" mode represents the opposite situation, wherein the fluid flows left (right) even though the droplet is near the right (left) outlet (Video S2, in Supplemental Material [37]). Oscillation means that the EGaIn droplet reciprocates quickly along the horizontal or vertical direction. Deformation refers to the change in the curvature of the EGaIn droplet/electrolyte interface. Zavabeti *et al.* [20] and Beni *et al.* [38] attribute this phenomenon to the pressure difference between the two sides of the curved interface. However, the interfacial deformation caused by the normal pressure gradient has little effect on overall fluid pumping behavior because of the action of the tangential electrocapillary force. Thus, it is not studied further in this paper.

A. Marangoni flow

Electrolyte solution pumping is caused by nonlinear electrocapillary stress at the interface between the EGaIn droplet and electrolyte. In order to investigate the observed pumping effect more insightfully, we compare the theoretical predictions to the experimental micro-PIV results.

Based on the flow field in the 3D channel [Fig. 2(a)] and electrical-analogy Marangoni streaming on the *X*-*Y* cutting plane [Fig. 2(b)], when the EGaIn droplet is placed in the center of the chamber, the flow field averages in space to zero and there is no pumping effect. This result matches the low-conductivity solution analytical prediction at $f_{\mathrm{RC}}^{\mathrm{LM}} = \sigma_f/2\pi C_T R < f \leqslant \alpha \mathbf{E} C_{\mathrm{DL}}/\varepsilon_{ox}\sigma_f = f_{\mathrm{crossover}}$ (Table I). Fluid flow originates from a change in the interfacial tension. For the purpose of comparison, we calculated the ratio of the LMD/electrolyte solution interfacial tension to the initial interfacial tension, i.e., γ/γ_0, as shown in Fig. 2(a). It is not difficult to find that the interfacial tension distribution is symmetrical. Interestingly, when the droplet is placed on the right chamber outlet and other conditions remain unchanged, the electrocapillary effect produces a right-hand net flow of fluid within the channel, as displayed in Figs. 2(c) and 2(d). This situation is akin to the "+" pumping mode at $f_{\mathrm{RC}}^{\mathrm{LM}} < f \leqslant f_{\mathrm{crossover}}$ in Table I in the presence of an apparent surface oxidation effect. This phenomenon can also be demonstrated by the sharp decrease in droplet interfacial tension at the slit [Fig. 2(c)]. Surprisingly, the fluid began to flow in the opposite direction (towards the left chamber outlet) upon modulating the work parameters to $\sigma_f = 1.6$ S/m, $\phi = 7$ V, $f = 200$ Hz [Figs. 2(e) and 2(f)]. The high-conductivity solution makes the field-induced oxide layer nearly disappear at high frequencies, resulting in subtle modulation of the interfacial tension gradient [Eqs. (10) and 12(a)]. This produces a situation similar to the "−" pumping mode at $f > f_{\mathrm{crossover}}$ in Table II. Comparison of Figs. 2(a), 2(c), and 2(e) indicates that the interfacial tension variation range in Fig. 2(e) is the smallest and there is almost no oxide skin involved. Besides, as the liquid conductivity and field frequency increase, the surface flow is induced by the interfacial tension gradient on the polarizable EGaIn droplet from divergent to convergent. This agrees with the analytical predictions in Tables I and II when the oxide layer is small [Eq. (4)].

Quantitative overviews of the ratio γ/γ_0 and the velocities along lines l_1, l_2, and l_3 on the EGaIn droplet surface are presented in Figs. 2(g) and 2(h), respectively. The abscissa is the x axis, which starts from the center of the chamber. We focus only on the interfacial tension gradient on the x axis, which is related directly to the fluid velocity in this direction. When the droplet is located in the center of the chamber, the curve of the ratio γ/γ_0 is an even function and its gradient is an odd function, consistent with the velocity distribution. The flow field on the surface of the left (right) hemisphere moves left (right) such that the electrocapillary eddies exhibit a diverging pattern with respect to the polar plane of the EGaIn droplet, even if no net pumping effect takes place. Electrolyte pumping occurs when the droplet is placed adjacent to the right chamber outlet.

The blue dotted line in Fig. 2(g) shows that the interfacial tension decreases sharply at the slit. This occurs because of the oxide layer formation and produces a pole at the corresponding position on the velocity curve [Fig. 2(h)]. Besides, on the curve of the ratio γ/γ_0 (the blue dotted line), the positive wave crest value is greater than the absolute value of negative trough. Thus, symmetry breaking in the nonlinear bipolar electrocapillary stress system pumps the fluid to the right. In the opposite situation, the oxidation effect is trivial in a high conductivity saline solution, and the interfacial tension varies within a small range, as shown in Fig. 2(g) by the

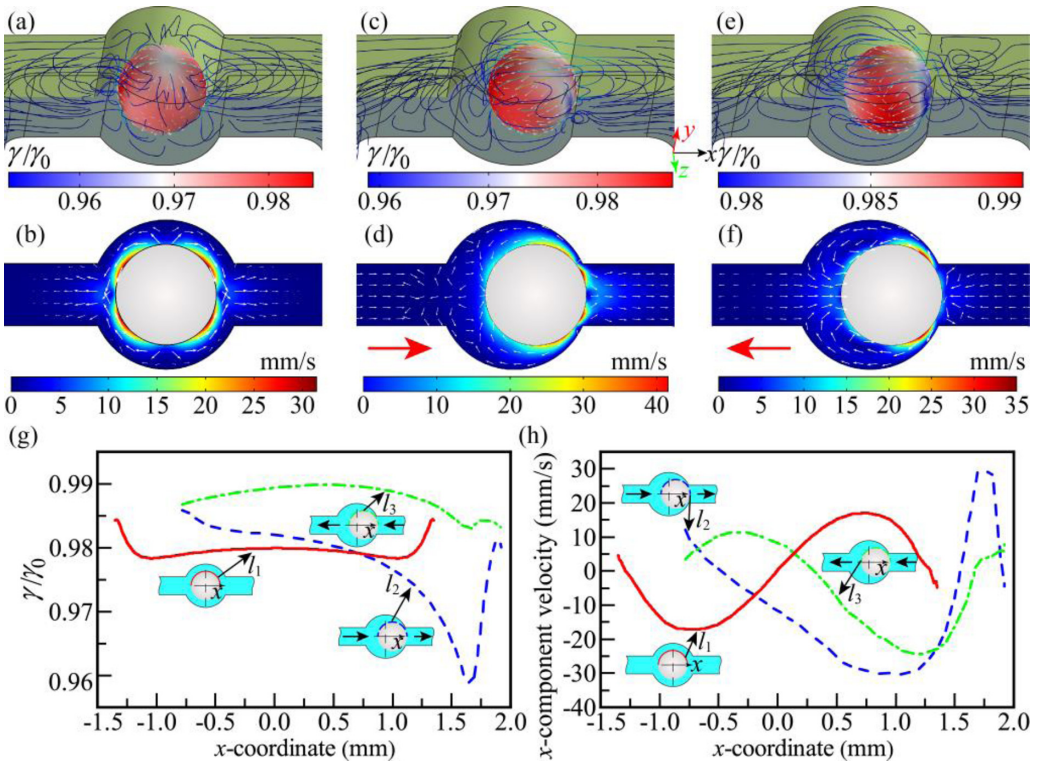

FIG. 2. Numerical simulation results of Marangoni flow field distribution when EGaIn droplet in different positions of the chamber, including the overview (the top row) and cross-sectional view (the middle row): (a) and (b) at the center, obtained with $\sigma_f = 0.5$ S/m, $\phi = 5$ V, $f = 100$ Hz; (c) and (d) near the right boundary, and the fluid flows to the right, obtained with $\sigma_f = 0.5$ S/m, $\phi = 5$ V, $f = 100$ Hz; (e) and (f) near the right side, and the fluid flows to the left, obtained with $\sigma_f = 1.6$ S/m, $\phi = 7$ V, $f = 200$ Hz; (g) the ratio γ/γ_o and (h) the surface flow velocity profiles along the lines l_1, l_2, and l_3, respectively.

green dash-dotted line. Domination by the nonlinear electrical stress produces a pair of vortices that converge around the droplet, as shown in Fig. 2(f) by the green dash-dotted line. The electric field is intensified locally within the narrow gap between the EGaIn droplet and the right chamber outlet. Thus, there is strong electrocapillary stress on the surface of the right hemisphere, and the net fluid motion is oriented from right to left.

To verify these simulations further and clarify the underlying pumping mechanism, the velocity field is visualized utilizing a micro-PIV apparatus. However, the nonuniform electric field interacts with the induced effective dipole moment of the tracer particles in the Marangoni flow, causing the particles to be subjected to the dielectrophoretic force [48]. The dielectrophoretic force is proportional to the particle volume and the gradient of the field magnitude squared [49–51]. Thus, the tracer particles motion can be influenced by the electric field. We analyze the influence of the dielectrophoretic force on the tracer particle trajectories in Supplemental Material [37]. The results show that the dielectrophoretic velocity of the particles is too weak to affect their course and can be ignored. The experimental demonstration of the flow field on and around the EGaIn droplet surface, as recorded via micro-PIV, is presented in Figs. 3 and 4 (Videos S3 and S4, in Supplemental Material [37]). Since the droplet diameter is 2.7 mm, which is much larger than the depth of field of the high-speed camera, we focus only on the flow field where the droplet diameter is largest. Limited by the field of vision of the camera, we divide the droplet into two parts, with the red dotted line in Fig. 3(a) as the dividing line. That is, we divide the system into the head of the upper (left) hemisphere and the tail of the lower (right) hemisphere. Upon superimposing multiple image sequences using IMAGEJ software, it is clear that there are vortices at both the droplet head and tail, as shown in Figs. 3(b) and 3(c). The experimental flow velocity vectors and contours can be acquired using PIV-processing software and are presented in Figs. 3(d) and 3(e). A pair of vortices move in counter-rotating directions on either side of the EGaIn droplet, respectively. Since both pair of vortexes converge on the EGaIn droplet surface, flow moves in opposite directions on either side of the polarizable interface, and the flow velocity is higher at the tail than that at the head. This eventually leads to fluid flowing from the head to the tail overall. This is presented as the "+" pumping mode at $f_{\mathrm{RC}}^{\mathrm{LM}} < f \leqslant f_{\mathrm{crossover}}$ for a relatively low-conductivity solution with non-negligible surface oxidation in Table I.

When the ion concentration is higher (Fig. 4), the experimentally observed flow direction is reversed and the tracer particles are pumped from the tail to the head. That is, the "−" pumping mode at $f > f_{\mathrm{crossover}}$ for a relatively high-conductivity solution with a diminishing oxide layer is observed. The experimental observations in Figs. 3 and 4 are compatible with the numerical simulation results in Figs. 2(d) and 2(f), respectively.

Figure 5 illustrates the numerical velocity results in the center of the upper channel branch. These results originate

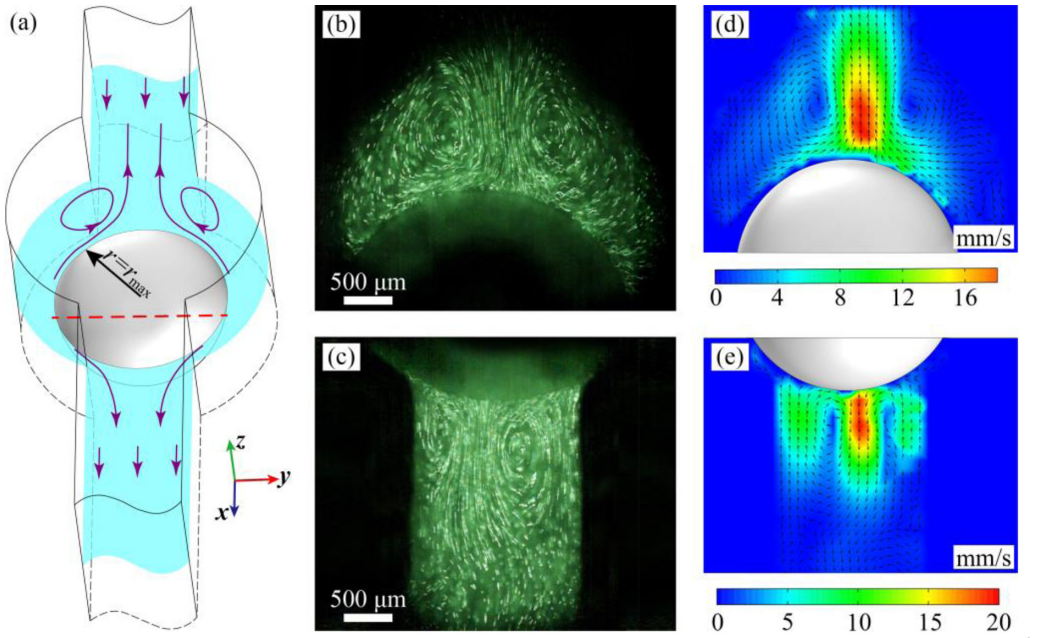

FIG. 3. Streamlines and velocity fields around the EGaIn droplet in NaOH solution with $\sigma_f = 0.5$ S/m, $\phi = 5$ V, $f = 100$ Hz (the "+" pump mode), located next to the right (lower) outlet of the chamber: (a) a sketch of the streamline contours around the droplet where the purple lines represent the streamlines; (b) and (c) are superimposed images of the tracer particles; (d) and (e) show velocity contours and vectors.

from ac field-driven Marangoni flow, as shown in Fig. 1(d), with the EGaIn droplet positioned adjacent to the chamber right outlet. We first explore the velocity distribution in the channel. Figure 5(a) shows the velocity profiles along the longitudinal direction under "+" pumping mode. The net flow propagates counterclockwise within the circular pump channel. The x-dependent flow speed fluctuates to a certain extent, so we calculated the average velocity along the blue line in Fig. 5(a) as the pumping speed. Figure 5(b) shows the vertical and lateral velocity profiles. Since the top of the channel is open to ambient air, the velocity profile along the channel depth direction is analogous to a logarithmic curve [green line in Fig. 5(b)]. On the other hand, the flow velocity manifests as a parabolic profile along the channel width direction. This is consistent with Poiseuille flow driven by an axial pressure gradient.

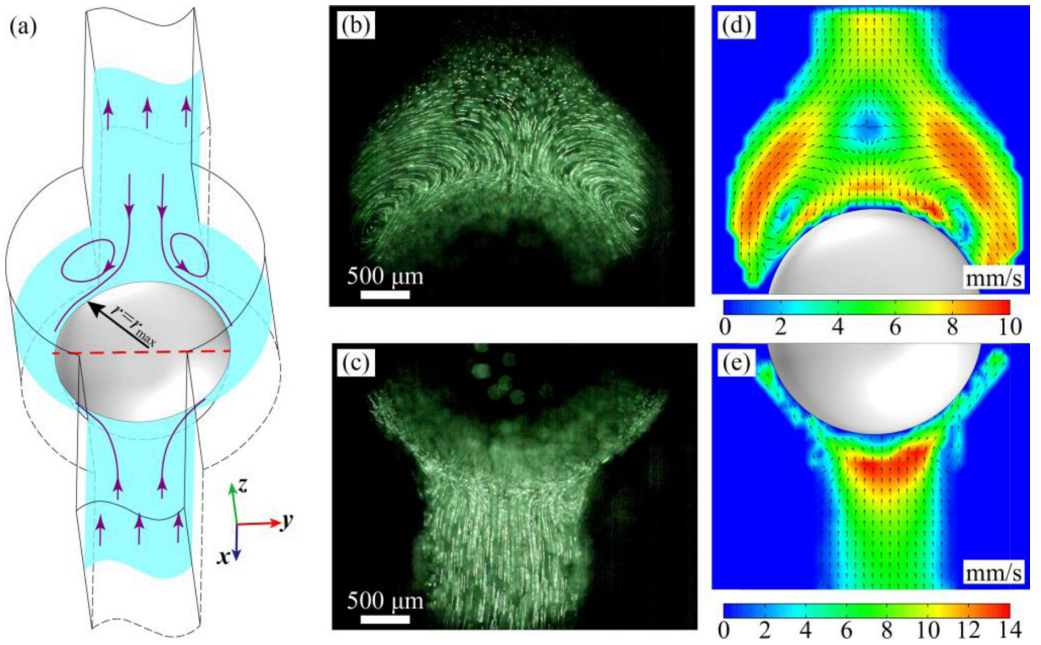

FIG. 4. Streamlines and velocity fields around the EGaIn droplet in NaOH solution with $\sigma_f = 1.6$ S/m, $\phi = 7$ V, $f = 200$ Hz, (the "−" pump mode), located next to the right (lower) outlet of the chamber: (a) a sketch of the streamline contours around the droplet where the purple lines represent the streamlines; (b) and (c) are superimposed images of the trapped particles; (d) and (e) show velocity contours and vectors.

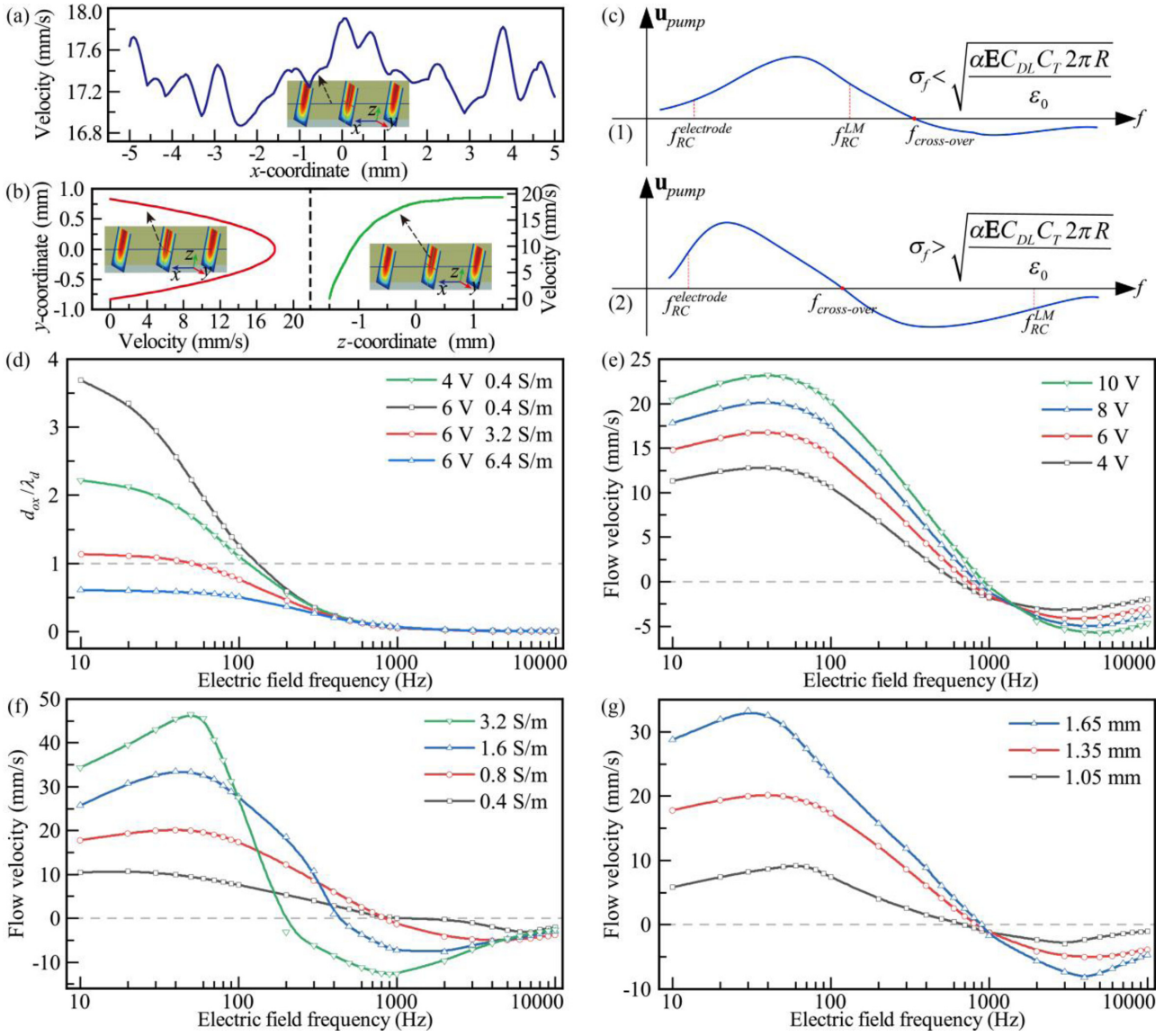

FIG. 5. Numerical simulation results of flow velocity: (a) and (b) profile velocity field along with the blue, red, and green cut lines in the inset, and the inset shows flow velocity profile in the channel, obtained with $\phi = 8$ V, $f = 100$ Hz, $\sigma_f = 0.8$ S/m, and $R = 1.35$ mm; (c) schematic diagram of the distribution positions of three characteristic frequencies at low conductivity (c1) and high conductivity (c2) respectively; (d) the variation of d_{ox}/λ_d with electric field frequency for various electrolyte conductivity; (e) flow velocity versus electric field frequency under different applied voltage, obtained with $\sigma_f = 0.8$ S/m and $R = 1.35$ mm; (f) flow velocity versus electric field frequency under different electrolyte conductivity, obtained with $\phi = 8$ V and $R = 1.35$ mm; (g) flow velocity versus electric field frequency under different droplet radius size, $\phi = 8$ V, and $\sigma_f = 0.8$ S/m.

The frequency-dependent pump behavior is presented qualitatively in Fig. 5(c) for low- and high-conductivity solutions. The results correspond to the analytical predictions in Tables I and II, respectively. First, in the low-conductivity situation, since the oxide layer thickness [Eq. (4)] exceeds the Debye length, the surface oxidation effect dominates within a wide frequency range, resulting in formation of a "+" pumping mode at $0 < f < f_{\text{crossover}}$ [Fig. 5(c1)]. The inhomogeneous thickness of the oxide layer is greater in the areas of larger electric field intensities. Because the more dominant role of the oxide layer over the double-layer capacitance, less voltage falls into the diffuse screening cloud where the field strength is strong. This is in contrast to the variation trend predicted by the conventional interfacial polarization model, which indicates that the induced zeta potential is larger where the electric field is greater. Therefore, under low electrolyte conductivity conditions, the presence of a nonuniform oxide layer changes the original direction of the double-layer voltage drop and the interfacial tension gradient. Then, the emergence of a "+" pumping mode can be predicted only by improving the traditional interfacial polarization model. Indeed, electrolyte pumping always occurs in the negative direction (not shown) when the surface oxidation effect is ignored as required by the traditional interfacial polarization model. In Fig. 5(c2), which presents a high-conductivity solution, the pumping mode recovers from "+" to "−" at a

higher frequency due to oxide layer shrinkage. Thus, bipolar-induced polarization dominates within a wider frequency range $f_{\text{crossover}} < f \leqslant f_{\text{RC}}^{\text{LM}}$. In this sense, it is necessary to revise the classical *RC* circuit model in order to predict the electrolyte pumping direction correctly as a function of the imposed field frequency.

Numerical simulations with various frequencies [Figs. 5(d), 5(e), 5(f), and 5(g)] were then performed to demonstrate the analytical trends in Fig. 5(c). We first analyzed the relationship between the ratio of the oxide layer thickness to the Debye length d_{ox}/λ_d and the electric field frequency at low and high conductivities. The oxide layer thickness varies continuously along the LMD surface since it depends sensitively on the local electric field strength, which is distributed unevenly around a LMD position offset. Hence, the oxidation thickness presented in Fig. 5(d) is the reference value calculated using the background space-maximum field intensity. The thickness of the oxide layer increases with the increment of the driving voltage amplitude when the conductivity remains constant. In order to reduce the influence of the oxidation effect, a higher frequency is required. When the same amplitude is applied, the oxide effect is dominant across a wide frequency range ($d_{ox}/\lambda_d > 1$) at low conductivity, but the oxide layer thickness decays rapidly with the frequency at high conductivity. This is consistent with the conclusion of theoretical analysis. By further increasing the conductivity, even at low frequencies, the oxide layer becomes very thin due to the alkaline solution with high conductivity dissolves the oxide layer more quickly. In Fig. 5(e), the frequency-dependent pump speed is plotted at various ac voltage amplitudes. The transition frequency at which the pump motion reverses direction increases with the applied voltage, which agrees qualitatively with the analytical expression $f_{\text{crossover}} \propto \mathbf{E}$. The pump flow velocity increase with voltage under the "+" and "−" pumping modes, in which the oxide layer and bipolar-induced polarization, respectively, play essential roles in the solution driving force.

The frequency-dependent pump velocity curves for distinct ion conductivities between 0.4 and 3.2 S/m are presented in Fig. 5(f). The transition frequency decreases with the ion concentration ($f_{\text{crossover}} = \alpha \mathbf{E} C_{\text{DL}}/\varepsilon_{ox}\sigma_f$). The stable pump speed of the "+" pumping mode at the low-frequency plateau increases with the solution conductivity. This indicates that the role of the oxide layer becomes less important and thus more voltage drops across the double layer. Surprisingly, the high-frequency plateau produces almost identical pumping velocities at different conductivities [Fig. 5(g)]. This occurs because the nonlinear bipolar electrocapillary stress term $2\mathbf{E}^2 x/(1 + (\omega C_T R/\sigma_f)^2)$ in Eq. (12a) has a value of $\mathbf{E}^2 x$ at $f_{\text{RC}}^{\text{LM}} = \sigma_f/2\pi C_T R$ that is independent of the solution conductivity.

The effect of the EGaIn droplet diameter on the resulting pump behavior is investigated via direct numerical simulation in Fig. 5(f). The transition frequency changes slightly with the droplet size because $f_{\text{crossover}} = \alpha \mathbf{E} C_{\text{DL}}/\varepsilon_{ox}\sigma_f$ is size independent. The flow velocities of both the "+" and "−" pumping modes increase with droplet size due to the induced polarization is enhanced. This is reflected by the distance factor x included in the numerator of Eq. (12a).

B. The effect of temperature

In addition to the electrocapillary effect, the equipment may experience Joule medium heating across the liquid layer since the highest conductivity and electrical potential used are 5.3 S/m and 10 V, respectively. The maximum temperature rise is calculated to be 2.95 K and reached between the electrode and the LMD. In contrast, the temperature around the LMD is relatively low because of the high thermal (26.6 W/m k) and excellent electrical (3.4×10^6 S/m) conductivities of EGaIn [9]. The actual temperature rise may be smaller if one considers convective heat transfer caused by electrocapillary flow. However, this will still cause three problems, including the change of fluid viscosity, ac electrothermal effect, and thermocapillary convection. When the conductivity of NaOH electrolyte is 5.3 S/m, the concentration is only 0.25 mol/l, so its viscosity can be regarded as that of water. According to the viscosity-temperature characteristic curve of water [52], it can be known that when the maximum temperature increases by 2.95 K its viscosity decreases from 1×10^{-3} to 9.3×10^{-4} Pa s. Through the simulation analysis, it is found that the viscosity gradient will raise the flow velocity. Still, it has little effect on the flow field, and the difference of the flow velocity does not exceed 5%, so the influence of temperature on viscosity can be ignored.

Besides, Joule heating caused by the nonuniform electric field produces both electrical conductivity and dielectric permittivity gradients in the medium. The action of the imposed ac field on these inhomogeneities exerts a volume force f_{ET} on the liquid, resulting in directed fluid transport. This phenomenon is termed ac electrothermal (ACET) flow. The time-averaged ACET body force can be obtained via a linear perturbation analysis [53,54]:

$$\langle f_{\text{ET}} \rangle = \frac{1}{2}\text{Re}\left(\frac{\varepsilon_f(\alpha_T - \beta_T)}{1 + j\omega\varepsilon_f/\sigma_f}(\nabla T \cdot \mathbf{E})\mathbf{E}^*\right) - \frac{1}{4}\varepsilon_f \alpha (\mathbf{E} \cdot \mathbf{E}^*)\nabla T, \tag{14}$$

where T is the temperature, $\alpha_T = (\partial\varepsilon_f/\partial T)/\varepsilon_f$, and $\beta_T = (\partial\sigma_f/\partial T)/\sigma_f$. For aqueous solutions at $T_0 = 293$ K, $\alpha_T = -0.004$ K^{-1}, and $\beta_T = 0.02$ K^{-1} [54]. Adding the electrical body force to the Navier-Stokes equation allows the fluid motion induced by the ACET effect to be determined.

The finite-element software COMSOL is used to solve electric, thermal, and velocity fields; see the Supplemental Material [37] for more details. The results of the thermal and fluidic simulations are shown in Figs. 6(a) and 6(b), where the length and color of each arrow are related to the ACET fluid velocity. Since the velocity is affected by the electric field strength and temperature gradient, the ACET flow velocity around the electrode is relatively large, with typical velocities of approximately 0.1 μm/s, as shown in Fig. 6(a). The electrocapillary velocity is on the order of 1 mm/s. Thus, the fluid transport velocity caused by ACET is at least 4 orders of magnitude smaller and is therefore negligible. The ACET flow velocity is a function of the field frequency, even at frequency ranges that are lower than the characteristic charge relaxation frequency $f_{M-W} = \sigma_f/2\pi\varepsilon_f = 1.19$ GHz of the liquid bulk. At a high frequency $f = 1$ MHz, the LMD recovers from an insulator to a perfect conductor from the perspective of an

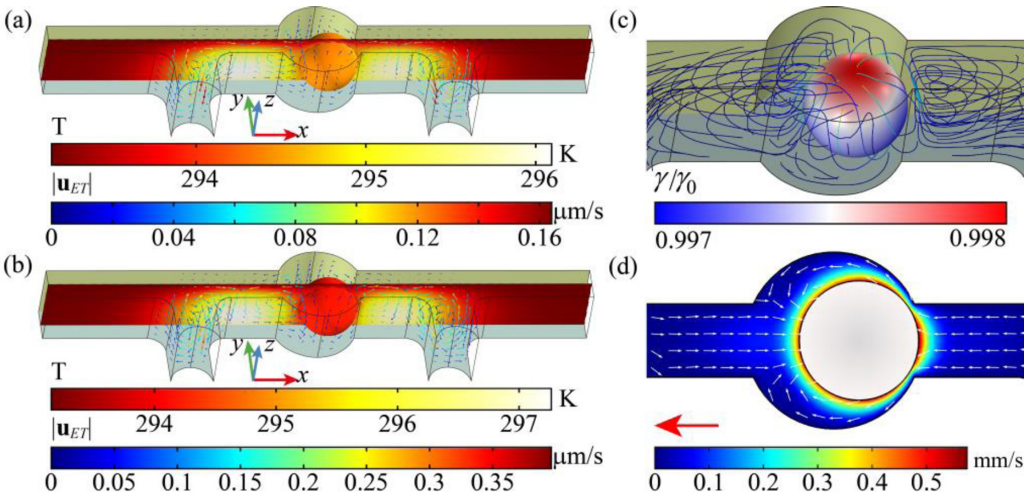

FIG. 6. Simulation results for the temperature (cut plane plot) and ACET velocity field (arrows) for $\phi = 10$ V, $\sigma_f = 5.3$ S/m, and (a) $f = 500$ Hz, (b) $f = 1$ MHz; the thermocapillary field distribution of (c) the overview and (d) cross-sectional view, obtained with $\sigma_f = 5.3$ S/m, $\phi = 10$ V, and $f = 500$ Hz.

observer. Consequently, more voltage drops across the liquid solution between the LMD and electrode probes, increasing both the temperature rise and ACET flow velocity compared to the low-frequency condition, as shown in Fig. 6(b).

Thermocapillary convection occurs when the interfacial tension depends on the temperature distribution, another form of Marangoni flow [55]. The previous numerical simulation results show that the maximum temperature rise is 2.95 K, so it is necessary to analyze the thermocapillary effect. Because the temperature variation range is small, the interfacial tension decreases nearly linearly with increasing temperature. The tangential stress is given by

$$\tau_T = -c_\gamma \nabla_t T, \tag{15}$$

where c_γ is the temperature coefficient of interfacial tension and $\nabla_t T$ is the tangential temperature gradient at the LMD/electrolyte interface.

Coupling electric, temperature, and flow field, combined with the Marangoni effect multiphysics coupling interface of software COMSOL, the simulation results are shown in Figs. 6(c) and 6(d). The distribution of interfacial tension is opposite to the temperature gradient, so the interfacial tension on the upper side is more significant than that on the lower side, as shown in Fig. 6(c). The cross-sectional view is displayed in Fig. 6(d). Obviously, the fluid flows to the left as a whole. However, because the direction of the temperature gradient remains constant, the movement of thermocapillary flow does not change even if the experimental parameters are changed, which is unlike the pump-direction-controllable electrocapillary flow considering the oxide layer. More importantly, the thermocapillary flow velocity is in the order of 0.1 mm/s, which is at least 10 times different from the experimental flow velocity scale. This proves once again that the ac electrocapillary stress is the most critical cause of fluid flow.

C. Oscillation behavior of EGaIn droplet

A previous study showed that the EGaIn droplet oscillates along the direction of the electric field line in an externally applied ac electric field [33]. In our experiment, two distinct modes of oscillation can be distinguished by simply altering the signal frequency, as shown in Fig. 7. At low field frequencies from 10 to 50 Hz (the thresholds fluctuate due to the voltage amplitude and conductivity), we find via experimental observation that the droplet can oscillate along the horizontal direction (the chamber length direction), as shown in Fig. 7(a) and Video S5 (in Supplemental Material [37]). The inertial relaxation time [56] of the electrolyte along the length direction of the small-scale channel is given by $T_x = \rho {L_x}^2/\eta = 0.01$ s, where $L_x = 0.1$ mm denotes the characteristic distance scale along with the axial extension of the EGaIn droplet. The fluid bulk has enough time to respond to the ac electrocapillary stress using a half period that exceeds 0.01 s, namely $2T_x \geqslant 0.02$ s and $f \leqslant 50$ Hz. Thus, field frequencies no more than 50 Hz can actuate an oscillating component of the interfacial electrocapillary stress [Eq. (12b)] that fluctuates at the electric field frequency. This matches well with the inertial relaxation time of the fluid bulk and results in periodic oscillation of the EGaIn droplet along the chamber length direction.

As for the second fluid oscillation mode, because of the requirement that $f \leqslant \eta/2\rho {L_y}^2$, if the typical length scale $L_y = 0.071$ mm along the chamber width direction, the excitation frequency should not exceed 100 Hz. This accords well with our experimental observation that the EGaIn droplet tends

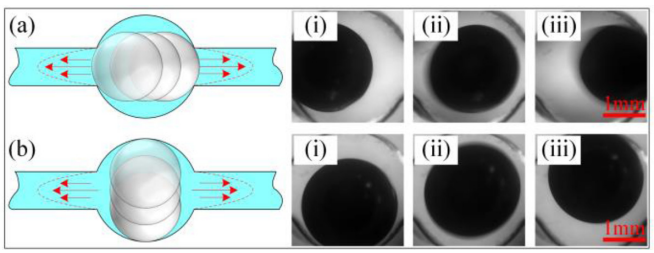

FIG. 7. Oscillation of EGaIn droplet at different frequencies with $\phi = 10$ V, $\sigma_f = 0.5$ S/m, $R = 1.35$ mm: (a) left and right oscillation of droplets at 10 Hz, (b) up and down oscillation of droplet at 10 Hz.

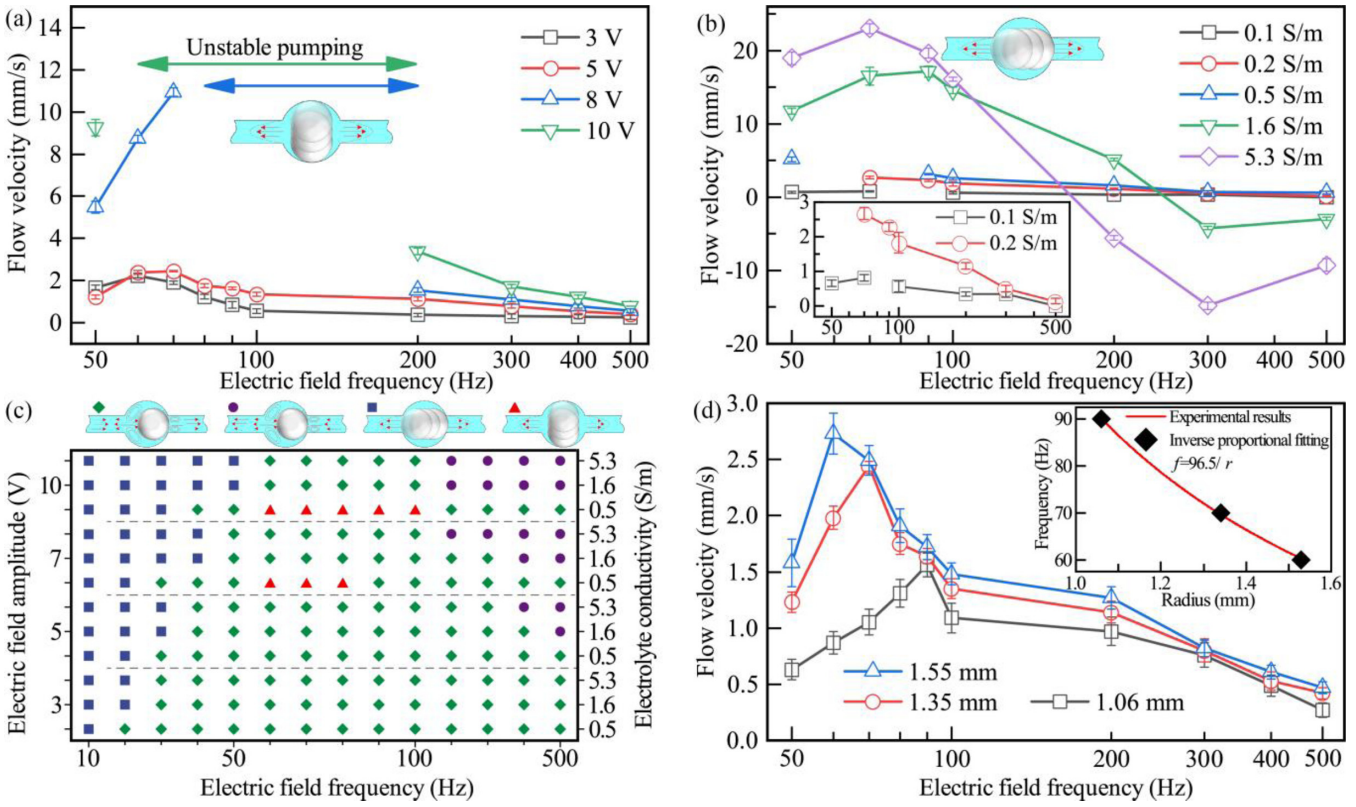

FIG. 8. Effects of the parameters on the flow velocity: (a) flow velocity against the electric field frequency for different applied voltage, obtained with $\sigma_f = 0.5$ S/m and $D = 1.35$ mm; (b) flow velocity against the electric field frequency for different electrolyte conductivities, obtained with $\phi = 7$ V and $R = 1.35$ mm; (c) summary of the law of the evolution of pumping performance under different electric field frequency, voltage and electrolyte conductivity; (d) flow velocity against the electric field frequency for different droplet radius, obtained with $\phi = 5$ V and $\sigma_f = 0.5$ S/m. The inset shows the relationship between the optimum frequency of pumping and the droplet radius.

to oscillate along the vertical direction (the chamber width direction) within the frequency range $60 \leqslant f \leqslant 100$ Hz, as shown in Fig. 7(b) and Video S6 (in Supplemental Material [37]). It is assumed that all droplet and adjacent fluid bulk oscillation behavior is caused by the second-order harmonic stress [Eq. (12c)], not its first-order counterpart [Eq. (12b)]. Although this presumption may not be entirely accurate, the resulting mathematical analyses are simplified and unified.

D. Pumping performance of EGaIn droplet under an ac electric field

Using an ac electric field to control the EGaIn droplet allows the electrocapillary flow velocity to be tuned precisely by many factors, including the ac signal parameters, droplet size, electrolyte conductivity, and electrolyte type. We next move on to investigate the effect that these features exerted on the flow velocity, as determined using the control variable method. The corresponding results are shown in Figs. 8 and 9.

First, we examine the influences of the field frequency (f), applied voltage (ϕ), and NaOH solution conductivity (σ_f) on the flow velocity. Figure 8(a) shows frequency-velocity curves at four different voltages when σ_f is fixed at 0.5 S/m. At low voltages ($\phi \leqslant 5$ V), as the frequency increases, the velocity rises to its maximum value and then decreases. That is, there is an optimum frequency between the electrode polarization frequency and flow reversal threshold, viz., $f_{RC}^{\text{electrode}} \leqslant f_{\text{optimal}} \leqslant f_{\text{crossover}}$. This is in good agreement with the simulation results in Fig. 5(e). The pump performance increases with the applied voltage since the interfacial oxidation effect dominates under "+" pumping mode. When the amplitude reaches 8 V, there are breakpoints at which unstable pumping occurs in the velocity-frequency curve. Upon observing the EGaIn droplet, we find that it exhibits a reciprocating vibration along the vertical direction. This is different from the vibration along the horizontal direction at ultralow frequencies, considering a good match between the half period of the ac signal and the inertial relaxation time of the bulk electrolyte.

In Fig. 8(b), the frequency-velocity curves are calculated for specific solution conductivities. The "−" pumping mode appears within the high-frequency range for liquid conductivities no less than 1.6 S/m. The pump performance increases with the solution conductivity under "+" pumping mode. The oxide layer thickness decreases, and thus there is a more significant voltage drop across the IDL at higher conductivities. Besides, under the high-frequency "−" pumping mode, the flow velocity decays with the frequency more slowly at higher solution conductivities. This occurs because the inverse RC relaxation time of the Debye layer $f_{\text{RC}}^{\text{LM}} = \sigma_f/2\pi C_T R$ increases with the ionic strength. In order to understand the effects of the electric field frequency, amplitude, and solution conductivity on EGaIn droplet behavior better, we performed

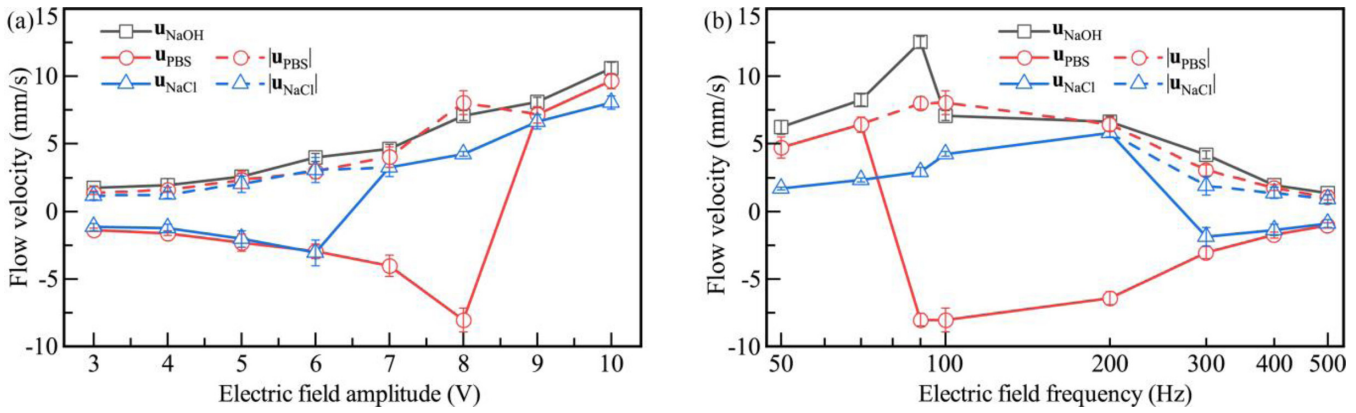

FIG. 9. Effect of electrolyte type on the flow velocity ($R = 1.35$ mm), where the dashed line represents modulus of the velocity: (a) flow velocity against the applied voltage, obtained with $f = 100$ Hz and $\sigma_f = 1.451$ S/m; (b) flow velocity against the electric field frequency, obtained with $\phi = 8$ V and $\sigma_f = 1.451$ S/m.

the simple summary shown in Fig. 8(c). The colored symbols in the figure represent the four droplet behavior states, that is, "+" pumping mode, "−" pumping mode, and the horizontal and vertical oscillation behaviors. At a low applied voltage of 3 V, in addition to experiencing low-frequency oscillating fluid motion, the electrolyte transports only in the "+" pumping mode, regardless of the solution conductivity. However, the "−" pumping mode begins to appear in the high frequency range at voltages no less than 5 V, and the flow reversal transition frequency decreases at larger voltage amplitudes and more excellent solution conductivities. Vertical oscillation of the EGaIn droplet tends to occur in an intermediate frequency range between 60 and 100 Hz when the voltage is considerable. The results are generally consistent with the influences of various parameters that were identified in our preceding analysis.

Next, the effect of the droplet size on the pumping velocity is discussed with other parameters kept constant ($\phi = 5$ V, $\sigma_f = 0.5$ S/m). As demonstrated in Fig. 8(d), the flow velocity increases with the droplet size under a given electric field and solution conductivity because the degree of electrochemical polarization at the EGaIn/electrolyte interface increases. Moreover, the experimental results indicate that the optimum frequency is inversely proportional to the droplet radius. The underlying reason is that the characteristic RC relaxation frequency is proportional to the reciprocal of the radius according to the previous analysis.

Finally, the influence of the electrolyte on the pumping performance was evaluated for three electrolyte types: NaCl, 1× PBS buffer, and NaOH. To compare the flow velocities, we measured the conductivity of 1× PBS buffer with a pH of 7.4 at 25 °C (1.451 S/m), and prepared separate NaCl and NaOH solutions with this standard conductivity. Experimental data on the relationship between the flow velocity and the applied signal (including the frequency and magnitude) are displayed in Fig. 9 with a fixed droplet size ($R = 1.35$ mm). The dotted line in the figure represents the modulus of velocity for the convenience of speed analysis. For these three electrolyte solutions, there is a slight deviation in diffusion coefficients ($D_{PBS} = 1.15 \times 10^{-9}$ m^2/s [57], $D_{NaCl} = 1.56 \times 10^{-9}$ m^2/s), and $\lambda_d \sim \sqrt{D}$ further weaken the influence on Debye length, causing the difference between the Debye lengths of the three solutions to be negligible. Thus, the flow velocity is affected mainly by the oxidized skin. The appearance of a thick oxide layer reduces the double-layer voltage drop and thereby the droplet interfacial tension gradient, resulting in decay of the flow velocity. Because the alkaline solution can dissolve Ga_2O_3, the stronger the alkalinity, the thinner is oxide layer. So, we measured the pH values of the NaOH and NaCl solutions to be 13.09 and 5.82 (deionized water is slightly acidic [58]). Obviously, the order of the electrocapillary pump flow velocities of the three solutions is consistent with that of the pH value, as shown in Fig. 9(a).

Besides, when the maintaining frequency is 100 Hz in PBS buffer, there is an extreme value at $\phi = 8$ V, and the flow direction reverses as the amplitude continues to increase, although the magnitude of the flow velocity typically increases with the applied voltage as a whole, as shown in the curve $|\mathbf{u}_{PBS}|$ in Fig. 9(a). Hence, we refer to the amplitude as the threshold voltage. It exists because of the competition between the oxide layer and the electric double layer. When the amplitude is low, the oxidation effect is weak. The electric double layer is dominant, the pump is in the "−" pumping mode, and the flow velocity increases with the amplitude. When the threshold voltage is exceeded, the oxidation effect takes the lead, causing the pump to switch to the "+" pumping mode. The flow velocity decreases due to the voltage division effect of the oxide layer. Upon further increasing the voltage, the oxide layer becomes thicker, but the electric potential drop across the double layer also increases accordingly. The flow velocity increases again, eventually leading to an extreme value of the flow velocity at the threshold voltage.

Figure 9(b) shows the flow velocity varies with the frequency in the three electrolyte solutions when the amplitude is fixed. The pumping directions produced by NaCl and the PBS buffer under low voltage or high frequency are positive. This is consistent with the influence of the oxide layer on the flow direction. The effects of electrical parameters on the oxide layer are more severe because the solution has a lower pH. In addition, since the liquid metal is easier to oxidize when the pH is low, a higher frequency is required to weaken the effect of oxidation. Hence, the optimal frequency decreases as the pH increases.

IV. CONCLUSIONS

In this work, we investigated the EGaIn droplet pumping phenomenon under a pure ac electric field in a closed-loop, open-top channel. This phenomenon was verified using micro-PIV technology and computational fluid dynamics (CFD). The results show that the pumping direction depended on the droplet position in the cylindrical chamber and the surface oxidation conditions. A formula for the varying thickness of oxide layer was established by combining our results with the previously reported electric-field-controlled mechanics of LMD surface oxidation. The formula was a function of the local voltage gradient, field frequency, and solution conductivity. The voltage division effect of the oxide layer changed the direction of the double-layer voltage drop square gradient and produced the "+" pumping mode; this was in sharp contrast to the "−" pumping mode created without the oxide layer. For high-conductivity ($\sigma_f > \sqrt{\alpha \mathbf{E} C_{\mathrm{DL}} C_T 2\pi R/\varepsilon_{\mathrm{ox}}}$) electrolytes, the pumping mode always changed from "+" to "−" at a variable transition frequency. Conversely, for low-conductivity ($\sigma_f < \sqrt{\alpha \mathbf{E} C_{\mathrm{DL}} C_T 2\pi R/\varepsilon_{\mathrm{ox}}}$) solutions, the large thickness of the oxide layer dominated electrocapillary stress generation. This produced the "+" pumping mode across a wide frequency band, and the "−" pumping mode was generally not observed experimentally. The platform was excited with only an ac electric field, which simplified the system, reduced the power consumption, and provided excellent low-conductivity solution pumping performance. It is envisaged that the superiority of our strategy owns broad application prospects, ranging from dynamic filtration to blood transport.

ACKNOWLEDGMENTS

This work is supported by the National Natural Science Foundation of China (Grants No. 12072096 and No. 11872165) and the Self-Planned Task (Grant No. SKLRS201803B) of State Key Laboratory of Robotics and System (HIT).

[1] M. Kim, D. K. Brown, and O. Brand, Nat. Commun. **11**, 1002 (2020).
[2] S. Chen and J. Liu, iScience **24**, 102026 (2021).
[3] R. Zhao, R. Guo, X. Xu, and J. Liu, ACS Appl. Mater. Interfaces **12**, 36723 (2020).
[4] B. Yao *et al.*, Chem. Eng. J. **410**, 128288 (2021).
[5] H. J. Mea, L. Delgadillo, and J. Wan, Proc. Natl. Acad. Sci. USA **117**, 14790 (2020).
[6] T. V. Neumann and M. D. Dickey, Adv. Mater. Technol. **5**, 2000070 (2020).
[7] M. Kim, H. Alrowais, C. Kim, P. Yeon, M. Ghovanloo, and O. Brand, Lab Chip **17**, 2323 (2017).
[8] J. Xu, Z. Wang, J. You, X. Li, M. Li, X. Wu, and C. Li, Chem. Eng. J. **392**, 123788 (2020).
[9] K. Khoshmanesh, S. Y. Tang, J. Y. Zhu, S. Schaefer, A. Mitchell, K. Kalantar-Zadeh, and M. D. Dickey, Lab Chip **17**, 974 (2017).
[10] L. Zhu, B. Wang, S. Handschuh-Wang, and X. Zhou, Small **16**, 1903841 (2020).
[11] E. Park, M. Lee, R. Phon, and S. Lim, Phys. Fluids **32**, 102002 (2020).
[12] W. Guo, A. J. T. Teo, A. M. Gañán-Calvo, C. Song, N. T. Nguyen, H. D. Xi, and S. H. Tan, Phys. Rev. Appl. **10**, 054045 (2018).
[13] H. Song, T. Kim, S. Kang, H. Jin, K. Lee, and H. J. Yoon, Small **16**, 1903391 (2020).
[14] X. Zhao, J. Tang, and J. Liu, Phys. Rev. Fluids **3**, 124804 (2018).
[15] Z. Yuan, X. Zhang, H. Hou, Z. Hu, X. Wu, and J. Liu, Phys. Rev. Fluids **5**, 111601 (2020).
[16] J. Wissman, M. D. Dickey, and C. Majidi, Adv. Sci. **4**, 1700169 (2017).
[17] X. Zhao, J. Tang, and J. Liu, Appl. Phys. Lett. **111**, 101603 (2017).
[18] S. Handschuh-Wang, Y. Chen, L. Zhu, T. Gan, and X. Zhou, Langmuir **35**, 372 (2019).
[19] L. Russell, J. Wissman, and C. Majidi, Appl. Phys. Lett. **111**, 254101 (2017).
[20] A. Zavabeti, T. Daeneke, A. F. Chrimes, A. P. O'Mullane, J. Zhen Ou, A. Mitchell, K. Khoshmanesh, and K. Kalantar-zadeh, Nat. Commun. **7**, 12402 (2016).
[21] S. Handschuh-Wang, Y. Chen, L. Zhu, and X. Zhou, ChemPhysChem **19**, 1584 (2018).
[22] M. R. Khan, C. B. Eaker, E. F. Bowden, and M. D. Dickey, Proc. Natl. Acad. Sci. USA **111**, 14047 (2014).
[23] S. Y. Tang, K. Khoshmanesh, V. Sivan, P. Petersen, A. P. O'Mullane, D. Abbott, A. Mitchell, and K. Kalantar-Zadeh, Proc. Natl. Acad. Sci. USA **111**, 3304 (2014).
[24] M. F. Wang, M. J. Jin, X. J. Jin, and S. G. Zuo, Phys. Chem. Chem. Phys. **19**, 18505 (2017).
[25] J. Xie, F. Li, S. Kuang, H. Yang, X. Li, S. Y. Tang, W. Li, and S. Zhang, IEEE-ASME Trans. Mechatron. **25**, 942 (2020).
[26] E. Wang, J. Shu, H. Jin, Z. Tao, J. Xie, S. Y. Tang, X. Li, W. Li, M. D. Dickey, and S. Zhan, iScience **24**, 101911 (2021).
[27] L. Yi, Q. Wang, and J. Liu, J. Phys. Chem. A **123**, 9268 (2019).
[28] P. Kumar, D. K. Verma, P. Parmananda, and S. Boccaletti, Phys. Rev. E **91**, 062909 (2015).
[29] D. K. Verma, H. Singh, P. Parmananda, A. Q. Contractor, and M. Rivera, Chaos **25**, 064609 (2015).
[30] Z. Yu, Y. Chen, F. F. Yun, D. Cortie, L. Jiang, and X. Wang, Phys. Rev. Lett. **121**, 024302 (2018).
[31] S. Y. Tang, V. Sivan, P. Petersen, W. Zhang, P. D. Morrison, K. Kalantar-Zadeh, A. Mitchell, and K. Khoshmanesh, Adv. Funct. Mater. **24**, 5851 (2014).
[32] R. C. Chiechi, E. A. Weiss, M. D. Dickey, and G. M. Whitesides, Angew. Chem. Int. Edit. **47**, 142 (2008).
[33] Y. Ren, R. Xue, W. Liu, Y. Tao, and F. Bao, J. Micromech. Microeng. **30**, 085007 (2020).
[34] Z. Sun, D. Sun, J. Hu, P. Traoré, H. L. Yi, and J. Wu, J. Electrost. **106**, 103454 (2020).
[35] D. Y. Li, X. B. Li, H. N. Zhang, F. C. Li, S. Qian, and S. W. Joo, Microfluid. Nanofluid. **21**, 10 (2017).
[36] I. Lazo, C. Peng, J. Xiang, S. V. Shiyanovskii, and O. D. Lavrentovich, Nat. Commun. **5**, 5033 (2014).
[37] See Supplemental Material at http://link.aps.org/supplemental/10.1103/PhysRevE.105.025102 for the first part features the

nomenclature; the second part features details of the experimental chip for pumping fluid (Fig. S1); the third part features relevant materials for the numerical solution of Marangoni flow (Figs. S2 and S3); the fourth part features the analysis of the effect of dielectrophoretic force on tracer particles (Fig. S4); the fifth part features relevant materials for the numerical solution of ACET (Fig. S5). Videos S1.avi and S2.avi show the fluid pumping phenomenon, Videos S3.avi and S4.avi show the experimental micro-PIV results, and Videos S5.avi and S6.avi show the EGaIn droplet oscillation.

[38] G. Beni, S. Hackwood, and J. L. Jackel, Appl. Phys. Lett. **40**, 912 (1982).

[39] A. Bonnefont, F. Argoul, and M. Z. Bazant, J. Electroanal. Chem. **500**, 52 (2001).

[40] C. K. Harnett, J. Templeton, K. A. Dunphy-Guzman, Y. M. Senousy, and M. P. Kanouff, Lab Chip **8**, 565 (2008).

[41] A. Ramos, *Electrokinetics and Electrohydrodynamics in Microsystems*, CISM Courses and Lectures Vol. 530 (Springer, Vienna, 2011).

[42] J. S. Kim, Z. Wu, A. R. Morrow, A. Yethiraj, and A. Yethiraj, J. Phys. Chem. B **116**, 12007 (2012).

[43] L. Junghoon and K. Chang-Jin, J. Microelectromech. Syst. **9**, 171 (2000).

[44] C. B. Eaker, D. C. Hight, J. D. O'Regan, M. D. Dickey, and K. E. Daniels, Phys. Rev. Lett. **119**, 174502 (2017).

[45] L. E. Scriven and C. V. Sternling, Nature (London) **187**, 186 (1960).

[46] R. Xue, W. Liu, T. Jiang, C. Song, H. Jiang, and Y. Ren, Adv. Mater. Interfaces **7**, 2000345 (2020).

[47] W. Liu, Y. Tao, Z. Ge, J. Zhou, R. Xu, and Y. Ren, Electrophoresis **42**, 950 (2020).

[48] V. Calero, P. Garcia-Sanchez, C. Honrado, A. Ramos, and H. Morgan, Lab Chip **19**, 1386 (2019).

[49] S. Park, Y. Zhang, T.-H. Wang, and S. Yang, Lab Chip **11**, 2893 (2011).

[50] W. M. Arnold, H. P. Schwan, and U. Zimmermann, J. Phys. Chem. **91**, 5093 (1987).

[51] S. Dash and S. Mohanty, Electrophoresis **35**, 2656 (2014).

[52] J. Kestin, M. Sokolov, and W. A. Wakeham, J. Phys. Chem. Ref. Data **7**, 941 (1978).

[53] A. Ramos, H. Morgan, N. G. Green, and A. Castellanos, J. Phys. D Appl. Phys. **31**, 2338 (1998).

[54] P. García-Sánchez, A. Ramos, and F. Mugele, Phys. Rev. E **81**, 015303 (2010).

[55] R. F. Probstein, *Physicochemical Hydrodynamics* (Butterworth-Heinemann, Oxford, 1989).

[56] T. M. Squires and S. R. Quake, Rev. Mod. Phys. **77**, 977 (2005).

[57] P. McConville and J. M. Pope, Polymer **41**, 9081 (2000).

[58] A. L. Mackie, Y. R. Park, and G. A. Gagnon, Environ. Sci. Technol. **51**, 10711 (2017).